LETTER
SPACE PHYSICS

Earth and Planetary Physics
2: 505–514, 2018
doi: 10.26464/epp2018049

Preliminary observation results of the Coherent Beacon System onboard the China Seismo-Electromagnetic Satellite-1

Liang Chen*, Ming Ou, YaPing Yuan, Fang Sun, Xiao Yu, and WeiMin Zhen

China Research Institute of Radiowave Propagation, Qingdao 266107, China

Abstract: This paper reports, for the first time, observation results of the Coherent Beacon System (CBS) onboard the China Seismo-Electromagnetic Satellite-1 (CSES-1). We describe the CBS, and the Computerized Ionospheric Tomography (CIT) algorithm program is validated by numerical experiment. Two examples are shown, for daytime and nighttime respectively. The Equatorial Ionization Anomaly (EIA) can be seen, and the northern crest core is located at ~20°N in the reconstruction image at 07:28 UTC on 20 July 2018 (daytime). Disturbances are shown in the reconstruction image at 18:40 UTC on 13 July 2018 (nighttime). We find that beacon measurements are more consistent with ionosonde measurements than model results, by comparing N_mF_2 at three sites at Lanzhou, Chongqing, and Kunming; consistency with ionosonde measurements validates beacon measurements. Finally, we have studied Vertical Total Electron Content (VTEC) variations from ground to ~500 km (the height of CSES-1 orbit) and ratios of VTEC between beacon measurements and CODE (Center for Orbit Determination in Europe) data. VTEC variation from ground to ~500 km has a range of 7.2–16.5 TECU for the daytime case and a range of 1.1–1.7 TECU for the nighttime case. The Beacon/CODE ratio of VTEC varies with latitude and time. The mean Beacon/CODE ratio is 0.69 for the daytime case and 0.26 for the nighttime case. The fact that the nighttime case yields lower ratios indicates the higher altitude of the ionosphere during nighttime when the ionosphere is assumed to be a thin layer.

Keywords: Coherent Beacon System (CBS); China Seismo-Electromagnetic Satellite-1 (CSES-1); Computerized Ionospheric Tomography (CIT); Total Electron Content (TEC)

Citation: Chen, L., Ou, M., Yuan, Y. P., Sun, F., Yu, X., and Zhen, W. M. (2018). Preliminary observation results of the Coherent Beacon System onboard the China Seismo-Electromagnetic Satellite-1. *Earth Planet. Phys.*, *2*(6), 505–514. http://doi.org/10.26464/epp2018049

1. Introduction

The China Seismo-Electromagnetic Satellite-1, also called ZhangHeng Satellite-1, was launched on 2 February 2018 at Jiuquan. Its mission is to monitor global space electromagnetic fields, ionospheric plasmas, high-energy particle deposition, and other physical phenomena. It provides a new technical means for seismic mechanism research, space environmental monitoring, and earth science research. The ionosphere is very important to people's life and space research. For example, ionospheric anomalies prior to earthquakes have been reported in many studies (Davies and Baker, 1965; Ondoh and Hayakawa, 1999; Liu JY et al., 2000; Chuo YJ et al., 2002; Popov et al., 2004; Liperovskaya et al., 2006; Dabas et al., 2007; Zhao BQ et al., 2008; Shen XH et al., 2011). Ionospheric disturbances such as ionospheric storms and scintillations have significant, adverse effects on increasingly sophisticated ground- and space-based technological systems (Buonsanto, 1999). With respect to space scientific research, substantial ionospheric data are needed to model the coupled ionosphere-thermosphere system and clarifying related mechanisms. However, the ionospheric parameters used in previous studies have been derived mainly from ground-based ionosonde data, topside sounding observations, and ground GPS receivers, which provide only the maximum electron density or limited coverage of ionosphere. The tomographic technique, which has become an important technique for academic and practical applications in various fields, can provide electron density distribution data on the global scale. In the recent past, many beacon satellites have been used as CIT signal sources, including the U.S. Navy Naval Navigation Satellite System satellites (NNSS), Radar Calibration (RADCAL) satellites, Defense Meteorological Satellite Program (DMSP) satellites, Russian Navigation Satellite System (RNSS) satellites, and Constellation Observing System for Meteorology, Ionosphere and Climate (COSMIC) satellites, through cooperation between the U.S. and Taiwan of China (Pryse and Kersley, 1992; Kunitsyn et al., 1994). Most of these studies have acquired ionospheric tomography images based on two-frequency beacon transmissions at VHF and UHF band frequencies. Bernhardt and Siefring (2006) illustrated that the three-frequency technique, using propagation of continuous wave signals at VHF, UHF, and L band frequencies, can yield more accurate absolute TEC than the two-frequency technique. The CBS onboard the CSES-1 was designed to transmit a series of phase-coherent signals on VHF/UHF/L bands (The work in this paper is based on two functioning frequency signals of VHF and L bands).

Austen et al. (1988) used the CIT algorithm to reconstruct the distribution of electron density with the TEC along the ray paths between the ground receivers and satellites. So far, many tech-

Correspondence to: L. Chen, crirp_cl@163.com
Received 24 AUG 2018; Accepted 09 NOV 2018.
Accepted article online 20 NOV 2018.

niques or inversion algorithms have been discussed to solve systems of linear equations (SLE) for ionospheric tomography reconstruction, including the special edition edited by Na HR (1994), the book by Kunitsyn and Tereshchenko (2003), and the review by Pryse (2003). The most commonly used algorithms based upon pixels include: the algebraic reconstruction technique (ART), the simultaneous iterative reconstruction technique (SIRT), and the multiplicative algebraic reconstruction technique (MART). MART has an advantage over ART (SIRT is an improved version of ART) in determining the electron densities, because it avoids unreasonable negative values (Hsiao et al., 2009). Thus, the MART inversion method has been selected, for now, as the CBS's default CIT algorithm.

This paper reports the first observational results of the CSES-1 CBS at mid-latitude and low-latitude of China. First, we briefly introduce the beacon observation system, including transmitter, ground receivers, and the network of ground stations. Second, we describe the MART inversion method, and the numerical experiment that has been carried out to validate the CIT program. Third, we reconstruct the ionospheric tomography images based on observational data and compare these to ionosonde data in order to assess the quality of CBS beacon measurements. Finally, we study VTEC variations based on the beacon measurements and ratios of VTEC between beacon measurements and CODE data.

2. Description of CBS Equipments and Station Network

The Coherent Beacon System of CSES-1 provides ionosphere products including TEC, distribution of electron density, and scintillation index (S4 index) and so on. The equipment of this system consist mainly of a transmitter onboard and receivers on the ground. The beacon transmitter sends a series of phase coherent radio signals of different frequencies to the ground receivers. It scans the ionosphere as the satellite moves horizontally. The electron density distribution is then reconstructed from the TEC along a set of rays. The schematic diagram of the ionospheric measurement from CBS is shown in Figure 1.

Principal components of the onboard beacon transmitter are an antenna and beacon transmitting unit, as shown in Figure 2. Main specifications of the beacon transmitter are listed in Table 1.

The beacon receivers receive beacon signals by a turnstile antenna. The ground receiver includes a receiving unit and antenna, as shown in Figure 3. Main Specifications of the beacon receiver are listed in Table 2.

The ground station network is composed of nine stations distributed in three provinces including Gansu, Ningxia, and Yunnan. The ground stations are located primarily in China's seismic belt. The distribution of the nine stations is given in Figure 4, and their geographical locations are listed in Table 3. The nine receivers can automatically receive signals transmitted from the beacon transmitter onboard CSES-1. Data collection, storage, and pre-processing are also implemented in the ground stations. Data files are sent in real time to the data center by the communication network. Five station chains are listed in Table 3, two for ascending orbits and three station chains for descending orbits. When the measurements of some ground receivers are severely affected by interference or have low SNR (signal noise ratio), the measurements data are discarded and the remaining ground receivers' measurements are used for reconstruction by the CIT algorithm.

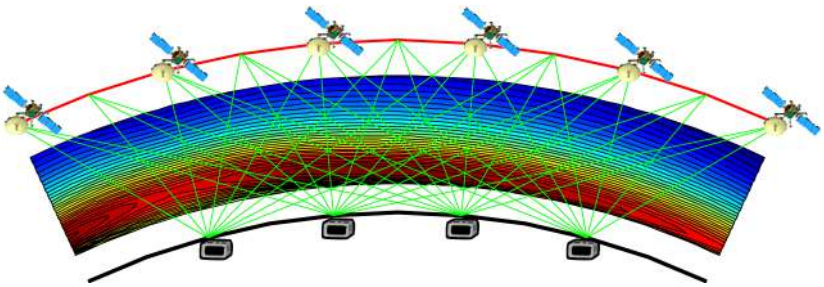

Figure 1. Schematic diagram of ionospheric measurement of the CBS.

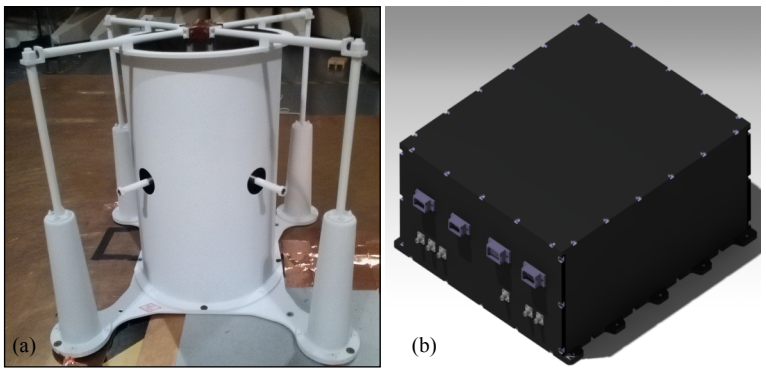

Figure 2. Transmitting antenna and transmitting unit of CBS. (a) Beacon Transmitting Antenna; (b) Beacon Transmitting Unit.

Table 1. Main specifications of the beacon transmitter

Transmitter Frequencies	VHF (150.*** MHz) UHF (400.*** MHz) L (1066.*** MHz)
Frequency Stability	≤5×10^{-11}/s
EIRP (I/Q)*(Effective Isotropic Radiated Power)	VHF≥1.5 dBW UHF≥1.5 dBW L≥4.0 dBW

* "I" is the in-phase component of the waveform, and "Q" represents the quadrature component.

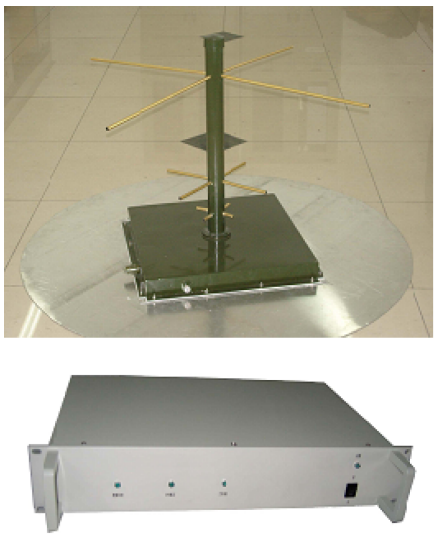

Figure 3. Receiving antenna and receiving unit of the CBS. (a) Beacon Receiving Antenna; (b) Beacon Receiving Unit.

Table 2. Main specifications of the beacon receiver

Received Frequencies	VHF (150.*** MHz) UHF (400.*** MHz) L (1066.*** MHz)
Sensitivity	≤–130 dBm
Dynamic Range	≥50 dB
Received Data	Phase and Amplitude
Sampling Rate	50 Hz

3. The CIT Algorithm and Validation with Numerical Experiment

The CIT algorithm aims to solve an inversion problem; the electron density distribution is reconstructed from a set of TEC measurements along the ray paths (Austen et al., 1988; Bernhardt et al., 2000; Ou M et al., 2012). A set of TEC measurements form the basic equation as follows,

$$\boldsymbol{Y} = \boldsymbol{H}x, \tag{1}$$

where $\boldsymbol{H}$ is an $m\times n$ normal matrix with h_{ij}, i=1, 2, …m and j=1, 2, …n, $\boldsymbol{Y}$ is a column vector of m measurements for STEC, x is a column of n electron density unknowns for cells in the targeted ionospheric region.

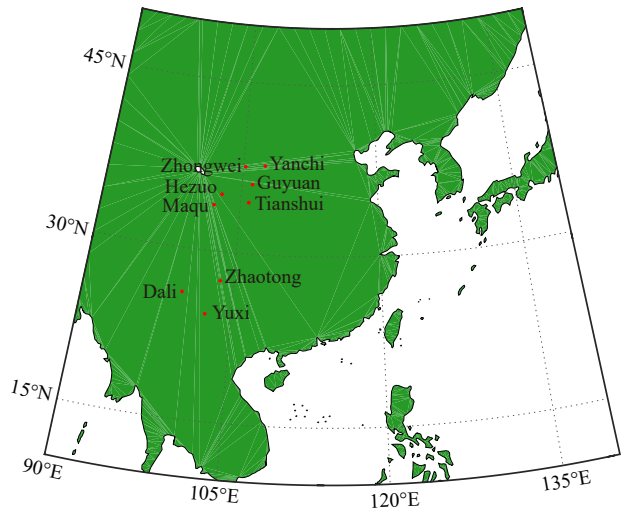

Figure 4. Distribution of the nine ground stations.

Table 3. Geographical locations of the ground stations

No	Station Name	Latitude (°N)	Longitude (°E)	Altitude (km)
1	Zhongwei	37.59	105.24	1.24
2	Yanchi	37.78	107.44	1.32
3	Guyuan	36.08	106.16	1.67
4	Hezuo	35.01	102.91	2.85
5	Maqu	34.02	102.17	3.42
6	Tianshui	34.48	105.90	1.16
7	Dali	26.14	99.94	2.04
8	Zhaotong	27.45	103.65	1.92
9	Yuxi	24.44	102.44	2.00

Table 4. Five station chains

No	Ground Stations of Each Chain	Note
1	Zhongwei, Hezuo, Maqu, Dali	Descending Orbit
2	Yanchi, Guyuan, Tianshui, Zhaotong, Yuxi	Descending Orbit
3	Dali, Zhaotong, Yuxi	Ascending Orbit
4	Hezuo, Maqu, Tianshui	Ascending Orbit
5	Zhongwei, Yanchi, Guyuan	Ascending Orbit

Three options for the CIT algorithm have been adopted in the CIT software applied to data from the CSES-1; they are (a) an algebraic reconstruction technique (ART), (b) a multiplicative algebraic reconstruction technique (MART), and (c) a simultaneous iterations reconstruction technique (SIRT); the default algorithm is MART. The MART algorithm used in the software is implemented as the following equation (2):

$$x_j^{k+1} = x_j^k \left(\frac{y_i}{\sum_{j=1}^{n} h_{ij} \times x_j^k} \right)^{\lambda_k \times h_{ij} \Big/ \sqrt{\sum_{j=1}^{n} h_{ij} \times h_{ij}}}, \tag{2}$$

where y_i is the ith absolute slant TEC (STEC) in a column of m measurements, x_j^k is the jth resulted cell electron density at the kth iteration with $0<\lambda_k<1$ (Hsiao et al., 2009), h_{ij} is the length of link i that lies in cell j. NeQuick model is served as an initial guess for the MART algorithm.

In the following we assess the inversion algorithm program by carrying out a numerical experiment. Figure 5 shows the flowchart algorithm used to reconstruct the electron density distribution. As shown in this flowchart, the sequence is that differential phase, observed relative STEC (the minima of STEC are set to zero), relative STEC in the equivalent orbital plane, absolute STEC in the equivalent orbital plane, and electron density distribution in the equivalent orbital plane are obtained successively.

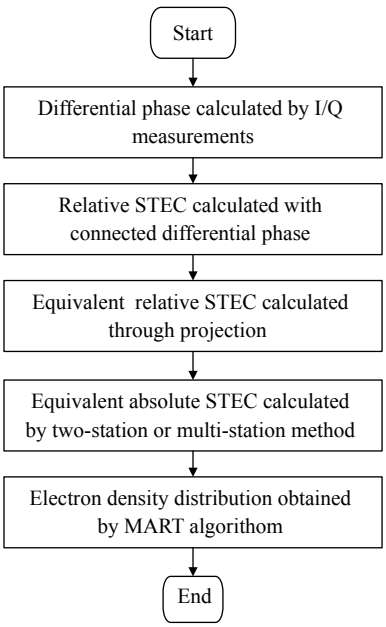

Figure 5. Flowchart of the algorithm for the reconstruction of electron density distribution in practice.

In the numerical experiment, we use NeQuick model to simulate "relative STEC observation". Firstly, the satellite positions at given times are calculated with the TLE (Two-Line Orbital Element) of CSES-1. Secondly, the simulated relative STEC observations are generated by the NeQuick model (the minima of STEC are set to zero) and are converted to STEC in the equivalent orbital plane (i.e. equivalent STEC). Figure 6 presents the simulation observations of equivalent relative STEC of four ground receivers at Yanchi, Guyuan, Zhaotong, and Yuxi on 20 July 2018. The simulated conditions, including locations of ground receivers and observation time, are the same as the first case in this paper. The footprint of the satellite, and the positions and elevations of the receivers can be seen in Figure 9. Next, the absolute TEC data are calculated by the two-station method (Leitinger et al., 1975) or the multi-station method (Leitinger, 1994). Figure 7 presents absolute STEC calculated by the multi-station method (solid lines) and simulation observations generated by the NeQuick model (dashed lines) of four ground receivers at Yanchi, Guyuan, Zhaotong, and Yuxi at 07:28 UTC on 20 July 2018. The maximum differences between solid lines and dashed lines are 1.0 TECU (Yanchi), 0.3 TECU (Guyuan), 1.7 TECU (Zhaotong), and 1.1 TECU (Yuxi) respectively.

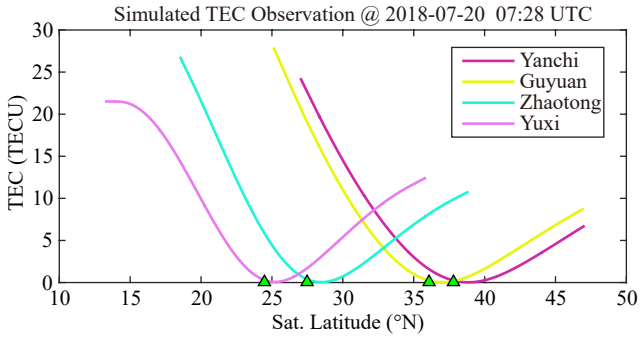

Figure 6. Simulation observations of equivalent STEC of four ground receivers at Yanchi, Guyuan, Zhaotong, and Yuxi at 07:28 UTC on 20 July 2018.

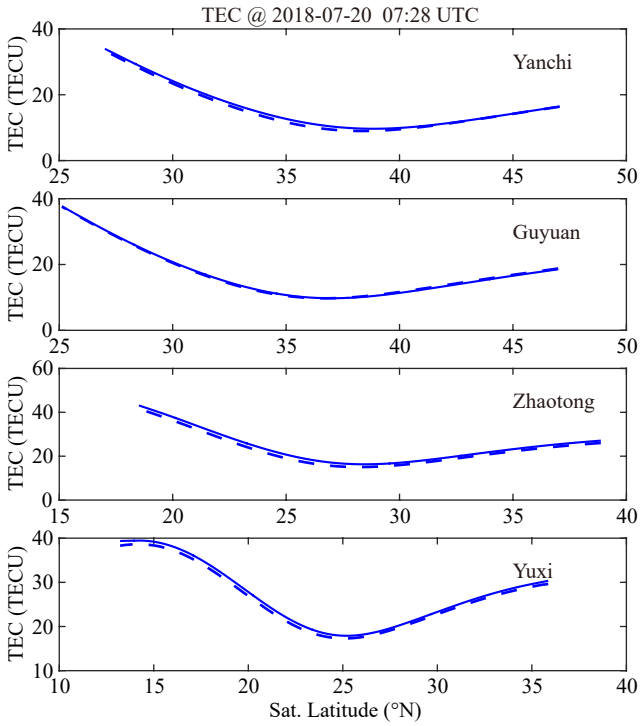

Figure 7. Absolute STEC of four ground receivers at Yanchi, Guyuan, Zhaotong, and Yuxi (from top to bottom) at 07:28 UTC on 20 July 2018. The sold lines denote absolute STEC calculated by the multi-station method. The dashed lines denote the simulation observations generated by the NeQuick model.

Finally, with absolute STEC calculated by multi-station method, the reconstructed ionospheric image can be obtained by the MART algorithm. Figure 8 presents the reconstructions using an initial guess with 20% deviation (top) and 40% deviation (middle) from the simulated electron density distribution observation (bottom) at 07:28 UTC on 20 July 2018. As shown in this figure, the heights of the northern crest cores of the three electron distributions are respectively 334.5 km (top), 334.5 km (middle), and 326.1 km (bottom). The electron densities of the northern crest cores are respectively 9.34×10^{11} m^{-3}, 9.52×10^{11} m^{-3}, and 8.80×10^{11} m^{-3}.

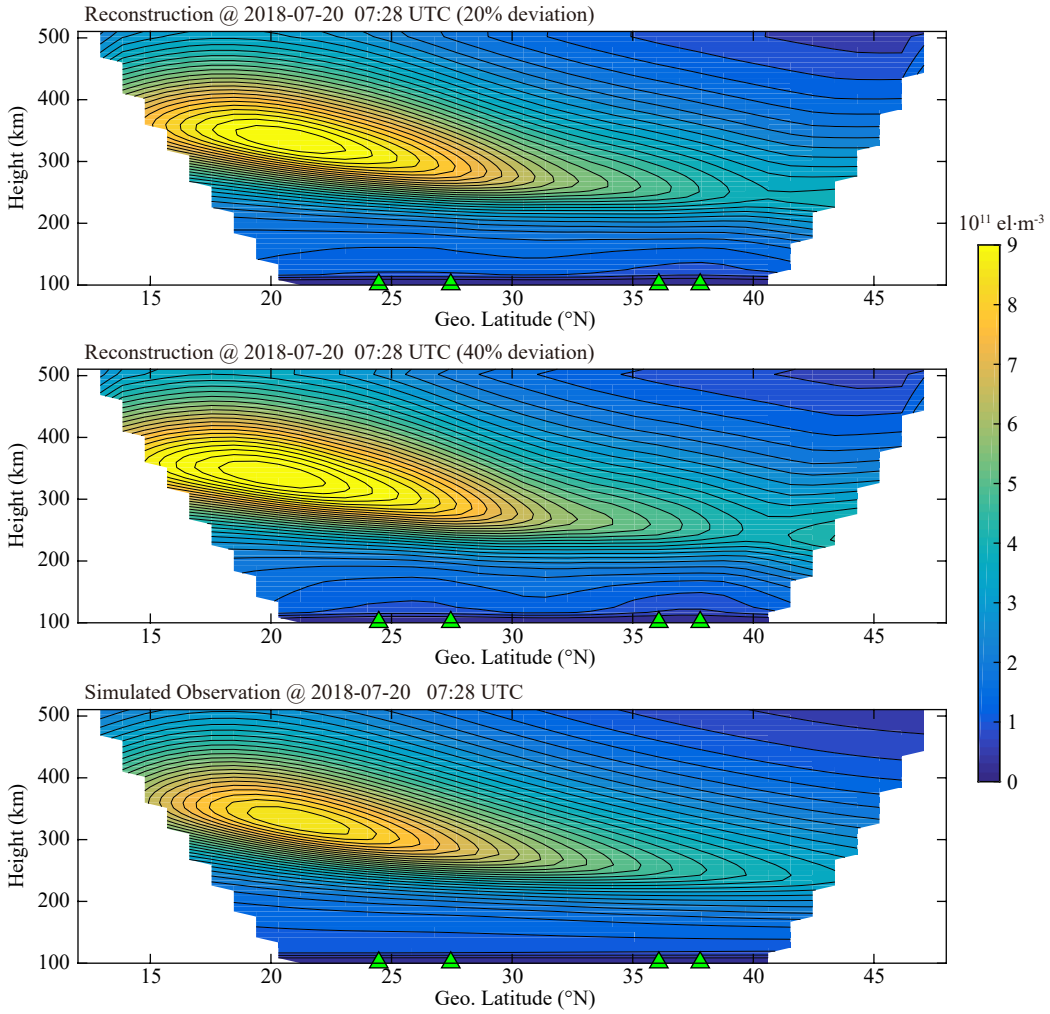

Figure 8. Reconstructions using an initial guess with 20% deviation (top) and 40% deviation (middle) from simulated observation generated by NeQuick (bottom) at 07:28 UTC on 20 July 2018.

Thus, the differences of heights and densities of the northern crest cores between the reconstructions (top and middle) and simulated electron density distribution (bottom) are 8.4 km and 0.56–0.72×10^{11} m^{-3} respectively. And the latitudes of the crest cores are all 21.2°N. Note that the altitude resolution of the density distribution is 8.4 km. That is to say, the differences in heights between the reconstructions (top and middle) and the simulated electron density distribution (bottom) are both less than 8.4 km. That the receivers and satellite orbit are not strictly in the same plane would cause error. Overall, the CIT algorithm program used in the system is proved to be effective. As seen in Figure 8, the reconstruction using an initial guess of 20% deviation is more consistent with "observation of density distribution" (simulated by NeQuick) than the reconstruction using an initial guess of 40% deviation. This result indicates that a large deviation of an initial guess would affect the reconstruction especially for the left and right edges of the electron density distribution, where the ray paths between satellite and receivers are relatively rare (please see Figure 1).

4. Preliminary Observation Results

In this section we present the preliminary ionospheric observation results from ground station receivers of two station chains, which correspond to descending orbit and ascending orbit, respectively. As the first example, we present a case of the satellite descending orbit at 07:28 UTC on 20 July 2018 (daytime). The location of the station chain is within mid-latitude and low-latitude. The station chain consists of four ground stations at Yanchi, Guyuan, Zhaotong, and Yuxi. Figure 9 (left) shows the footprint of the satellite at about 07:28 UTC (daytime) on 20 July 2018. The duration of this descending orbit shown in this figure lasts 9.0 minutes. The oblique line denotes the footprint of the satellite. The black straight line denotes the equivalent orbital plane, and the equivalent longitude is 104.3°E. The triangle symbols represent the positions of the four ground stations. Figure 9 (right) shows the elevation variations of the four ground receivers. The data when elevation was less than 15 degree have been discarded. The elevation variations plotted in the right figure have maxima of 66.6° (Yanchi), 73.9° (Guyuan), 76.4° (Zhaotong) and 82.6° (Yuxi) respectively.

The top panel in Figure 10 shows the projection of STEC measurements (i.e. the equivalent STEC) observed by the four ground receivers during this descending obit period. The bottom panel of this figure is the equivalent STEC simulated by the ionosphere model. It can be seen that the observed STEC has a high similarity

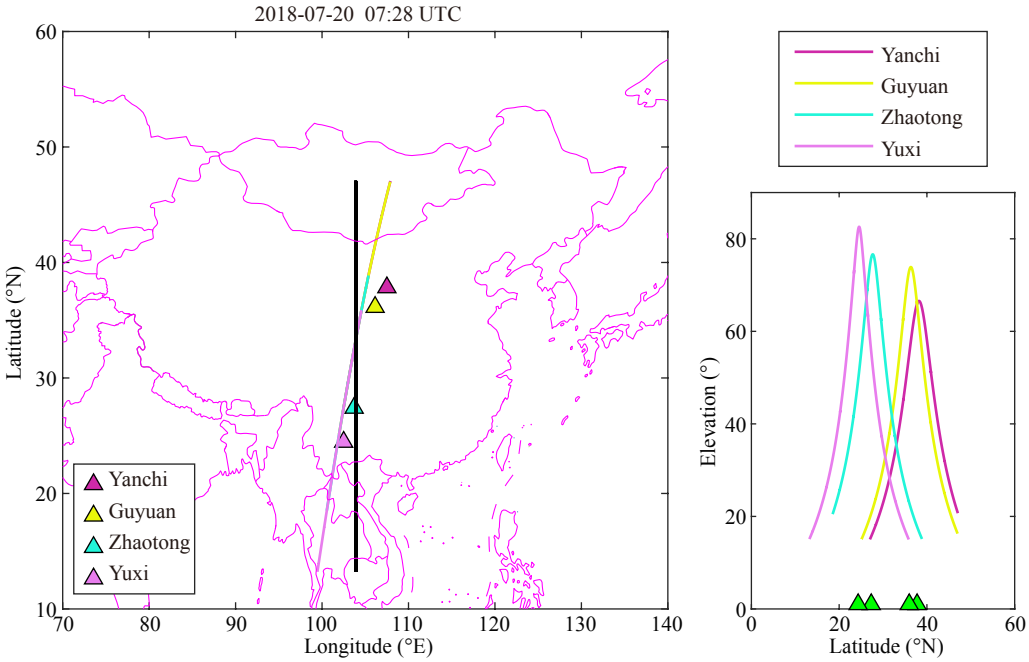

Figure 9. Footprint of the CSES-1 and receiver positions (left) and variation in elevation of the receivers with satellite latitude (right) at 07:28 UTC on 20 July 2018. The oblique line is the footprint of the satellite. The black straight line is the equivalent orbital plane.

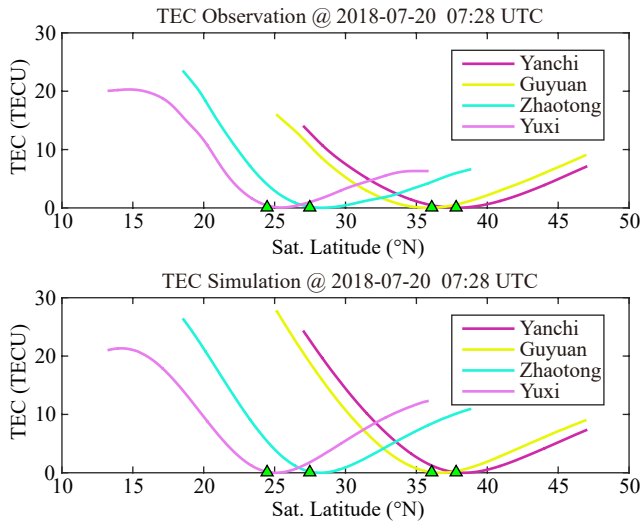

Figure 10. TEC observation (top) and TEC simulation generated by NeQuick (bottom) of the equivalent plane at 07:28 UTC on 20 July 2018.

with the STEC generated by the model, except that the relative STEC observations at the range from 25°N to 35°N are smaller than those of model results. The correlation coefficient between observation results and model results is 0.94.

Further, we use the MART inversion algorithm to obtain the electron density distribution. A typical example of a daytime reconstruction image is shown in Figure 11. EIA (northern crest) can be seen in the ionosphere reconstruction. The MART-generated electron density of the northern crest core is 8.13×10^{11} m^{-3}, at an altitude of 334.5 km and a latitude of 20.3°N: the electron density generated by the NeQuick simulation is 8.81×10^{11} m^{-3}, and the northern crest core has an altitude of 326.1 km and a latitude of 21.2°N. The maximum electron density of the top panel is smaller than that of the bottom panel. The latitude of the northern crest of the observation result is ~0.9° lower than that of the model result and the peak height of the reconstructed electron density distribution is 8.4 km higher than that of the simulation.

In the following, we present case of the satellite ascending orbit at 18:40 UTC on 13 July 2018 (nighttime). The station chain consists of two ground stations at Guyuan and Zhongwei. The left panel of Figure 12 shows the footprint of the satellite at about 18:40 UT on 13 July 2018. The duration of this ascending orbit in the figure is ~6.3 minutes. The oblique line is the footprint of the satellite. The black straight line is the equivalent orbital plane, and the equivalent longitude is 105.5°E. The triangle symbols represent the positions of the two ground stations at Guyuan and Zhongwei. The right figure presents the elevation variations of two receivers with the satellite latitude, which have maxima of 85.7° (Guyuan) and 88.6° (Zhongwei).

The top panel in Figure 13 shows the equivalent STEC observations from the satellite to the two ground receivers located at Guyuan and Zhongwei. The bottom panel shows the corresponding equivalent STEC variations simulated using the NeQuick model. As seen in this figure, the variations of relative STEC observed by the two ground receivers in the top panel are mostly smaller than those in the bottom panel at the same latitude. In addition, the two STEC variation curves are both symmetrical in the top panel, while the STEC variations in the bottom panel both have obviously larger TEC values at the range from ~25°N to ~36°N than those at the range from ~36°N to ~48°N. The correlation coefficient between observation results and model results is 0.87. The phenomenon of visible disturbances of the relative STEC variations in the top panel may be attributed to the low TEC values at night.

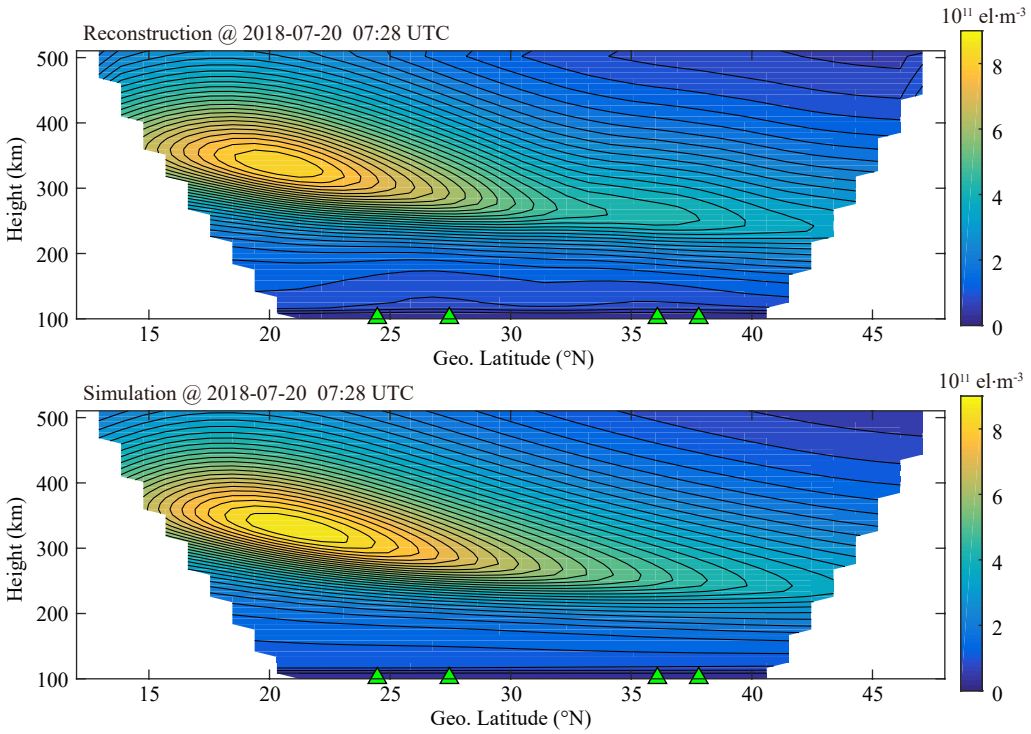

Figure 11. Reconstruction (top) and simulation (bottom) of the electron density distribution at 07:28 UTC on 20 July 2018.

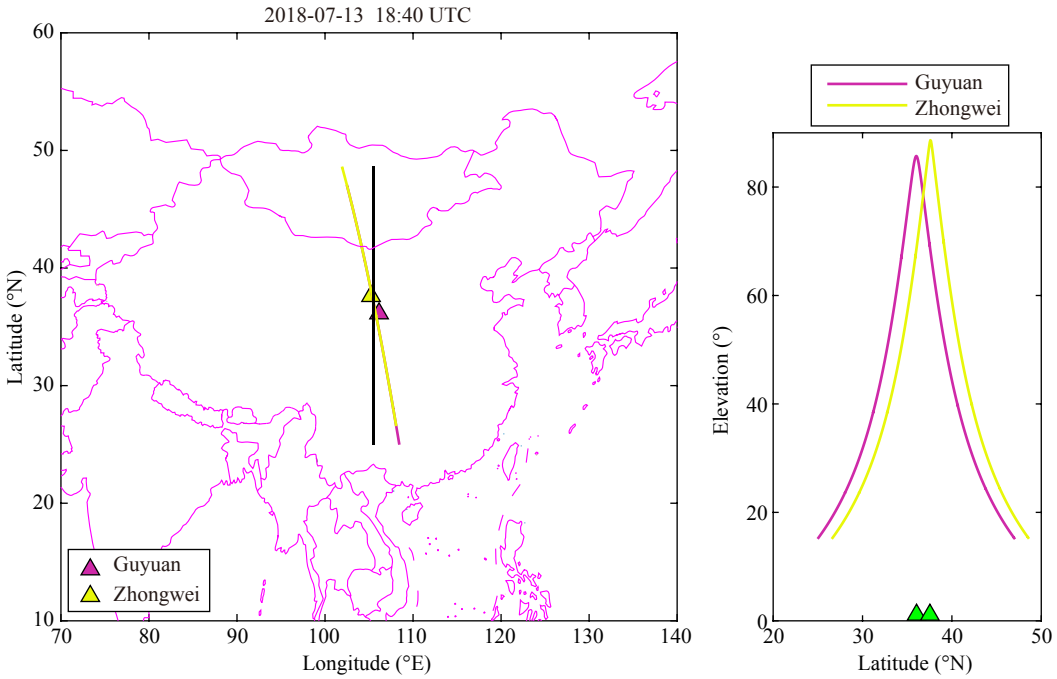

Figure 12. Footprint of CSES-1 and positions of receivers (left) and elevation of the receivers varies with satellite latitude (right) at 18:40 UTC on 13 July 2018. The oblique line is the footprint of the satellite. The black straight line is the equivalent orbital plane.

We next use the MART inversion algorithm to obtain the electron density distribution of this case. Figure 14 presents the reconstructed ionospheric electron density distribution (top) and background ionospheric electron distribution (bottom) at equivalent longitude of 105.5°E at 18:40 UTC on 13 July 2018. As seen in this figure, the reconstruction is different from the simulated electron density distribution generated by the ionospheric model. In the top panel, the F_2 layer has maximum ionospheric electron density at F_2 peak (N_mF_2) of 1.0–1.5×10^{11} m^{-3}, which is smaller than those of 2.0–2.5×10^{11} m^{-3} in bottom panel. In addition, the tendency of N_mF_2 in the top panel is different from that in the bottom where the N_mF_2 becomes smaller at higher latitudes. Disturbances of

N_mF_2 can be seen in the reconstructed electron density distribution. Note that in the top panel, densities at left and right edges of the density distribution are affected by larger initial electron densities where the ray paths between satellite and receivers are relatively rare (please see Figure 1).

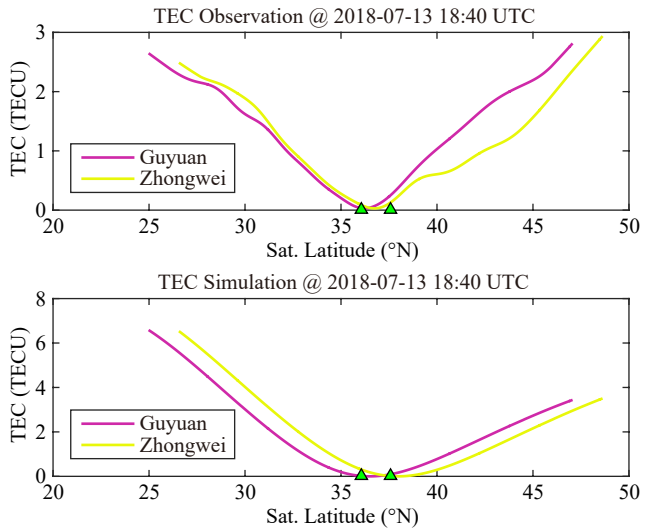

Figure 13. . Observations of TEC (top) and TEC simulation generated by the ionospheric model (bottom) at equivalent longitude of 105.5°E at 18:40 UTC on 13 July 2018.

In order to assess the beacon measurements, the N_mF_2 values from beacon measurements, ionosonde measurements, and model results at the same latitudes of the two cases are given in Table 5. We first acquire f_oF_2 (critical frequency of the F_2 layer) measurements of ionosondes located at Lanzhou (36.06°N, 103.87°E), Chongqing (29.51°N, 106.42°E), and Kunming (25.64°N, 103.72°E) on 20 July 2008 and 17 July 2008. Then, N_mF_2 ionosonde data are derived. N_mF_2 values of beacon measurements and model results of the three sites are also obtained by interpolation. The time differences between the beacon measurements and corresponding ionosonde measurements are within 30 minutes. As seen in this table, beacon measurements are more consistent with ionosonde measurements than model results. The consistency with ionosonde measurements validates the beacon measurements.

In order to depict the VTEC variation at different latitudes, Figure 15 shows the observations of VTEC versus latitude for the above two cases. As seen in the top panel, the four VTEC variations observed by the ground receivers are quite consistent with each other when available. The VTEC at the northern crest shown in this fig-

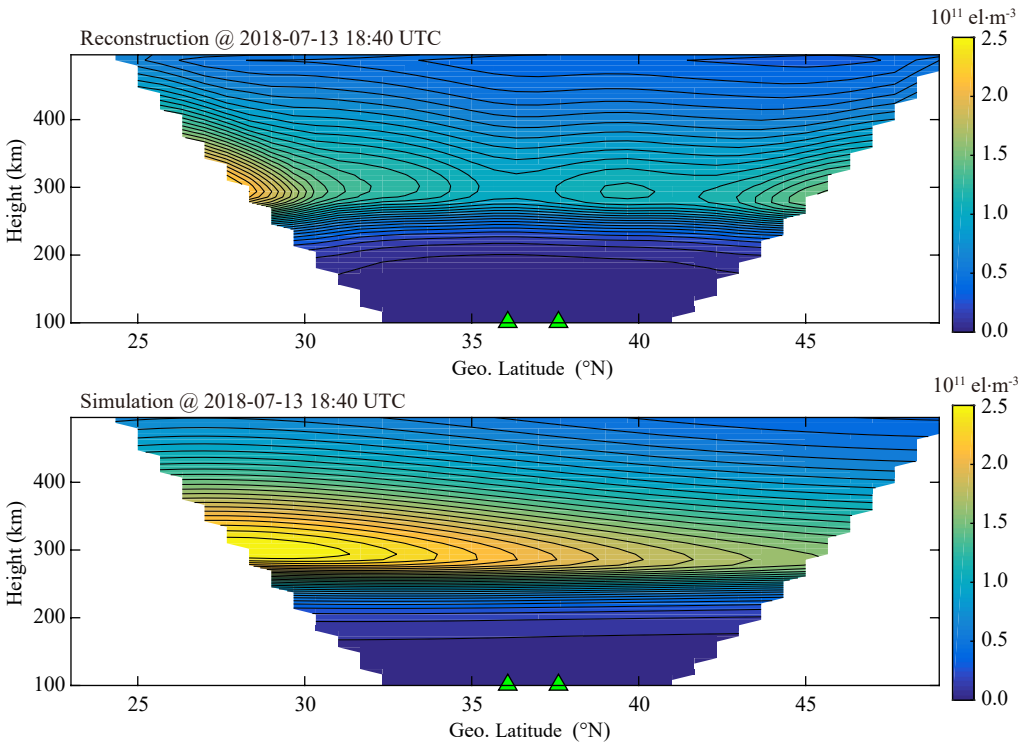

Figure 14. Reconstruction (top) and simulation (bottom) of electron density distribution at equivalent longitude of 105.5°E at 18:40 UTC on 13 July 2018.

Table 5. N_mF_2 comparison between CIT and Ionosonde results (unit: 10^{11} el·m^{-3})

	Lanzhou			Chongqing			Kunming		
	Beacon	Ionosonde	Model	Beacon	Ionosonde	Model	Beacon	Ionosonde	Model
2018-07-20	4.3	3.6	4.8	5.4	none	6.6	6.9	7.0	7.9
2018-07-13	1.0	1.0	2.1	1.8	1.7	2.5	None	None	None

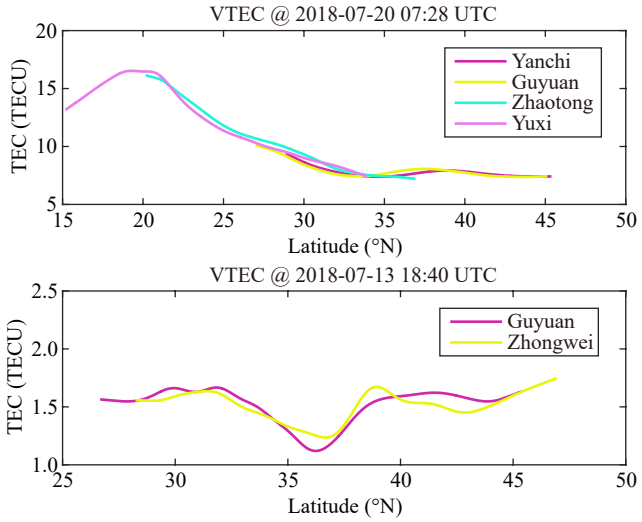

Figure 15. Observations of VTEC versus latitude at equivalent longitude of 104.3°E at 07:25 UTC on 20 July 2018 at Yanchi, Guyuan, Zhaotong, and Yuxi (top), and observations of VTEC versus latitude at equivalent longitude of 105.5°E at 18:36 UTC on 13 July 2018 at Guyuan and Zhongwei (bottom).

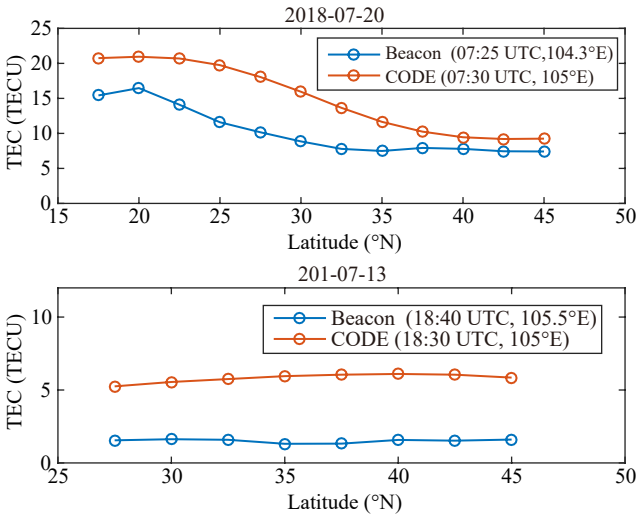

Figure 16. VTEC variations of beacon data and CODE data during the daytime on the 20 July 2018 (top) and during the nighttime on the 13 July 2018 (bottom).

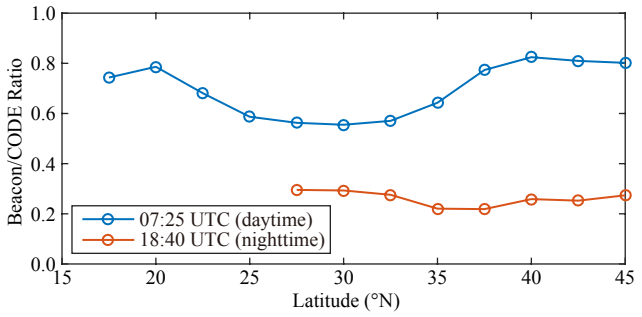

Figure 17. Beacon/CODE ratio of VTEC during the daytime on the 20 July 2018 (top) and the nighttime on the 13 July 2018 (bottom).

ure has a TEC of ~15 TECU at ~20°N. Then, the values decrease rapidly with higher latitude until ~30°N. The VTEC values retain 6.5 TECU at the range of latitude from ~35°N to ~45°N. As seen in the bottom panel, the two curves by the two ground receivers are also quite consistent with each other, and have TEC values of 1.0–1.7 TECU from ~26°N to ~47°N. The two VTEC variations for nighttime both have a trough from ~35°N to ~37°N and a bulge at ~39°N, which are in accord with those characteristics in Figure 14 (top).

Finally, we have studied ratios of VTEC between beacon measurements and CODE data. VTEC variations of beacon data and CODE data are first presented. As seen in Figure 16, the blue lines denote the average of the VTEC variations in top and bottom panels in Figure 15. The red lines denote corresponding VTEC variations of CODE data. In the top panel, the VTEC based on beacon measurements has a range of 6.8–15.0 TECU at 07:25 UTC at 104.3°E, while the VTEC (averages of VTEC values of 07:00 UTC and 08:00 UTC) based on CODE data has a range of 9.2–21.0 TECU at 07:30 UTC at 105°E. In the bottom panel, the VTEC based on beacon measurements has a range of 1.3–1.6 TECU at 18:40 UTC at 105.5°E, while the VTEC (averages of TEC values of 18:00 UTC and 19:00 UTC) based on CODE data has a range of 5.3–6.1 TECU at 18:30 UTC at 105°E. Note that the orbit of the CSES-1 has an altitude of ~500 km. That is to say the integral height of the upper limit of the VTEC derived from beacon measurements is ~500 km, while that derived from CODE data is ~20000 km. Figure 17 presents Beacon/CODE ratio of VTEC for the daytime on the 20 July 2018 (top) and the nighttime on the 13 July 2018 (bottom). As shown in this figure, the Beacon/CODE ratio of VTEC varies with latitude and time. The blue line in Figure 17 indicates Beacon/CODE ratio varies 0.56–0.82 (average of 0.69) over the range from 17.5°N to 45°N; over the range 27.5°N to 45°N, the Beacon/CODE ratio varies 0.22–0.30 (average of 0.26). The lower ratios of the nighttime case indicate higher ionosphere altitudes during nighttime, when the ionosphere is assumed to be a thin layer.

5. Summary

The China Seismo-Electromagnetic Satellite-1 is a newly developed space scientific research satellite, and is also the first satellite of the China geophysical field exploration satellite project. Through the monitoring of global space electromagnetic field, ionospheric plasma, high-energy particle deposition, and other physical phenomena, the satellite provides a new technical means for seismic mechanism research, space environmental monitoring, and earth system science research. The beacon transmitter equipped on the CSES-1 transmits a series of phase-coherent signals as the satellite moves horizontally. Receivers on the ground can receive the signals and generate data file of I/Q at the different frequencies. This paper has introduced the CBS aboard the CSES-1, including equipment and the network of associated ground stations.

A MART algorithm has been adopted as the CBS's default inversion method. It avoids unreasonable negative electron densities, which is an advantage over ART. This paper has introduced a MART inversion algorithm and carried out numerical experiments to assess the inversion algorithm. Simulations of observations of

relative STEC have been generated using the NeQuick model. Reconstructions with 20% and 40% deviations from a "real density distribution" are compared with the "real density distribution" generated by the NeQuick model. The results indicate that the CIT algorithm adopted in this paper is effective. Large deviations in an initial guess would affect the reconstruction, especially for the left and right edges of the electron density distribution, where ray paths between satellite and receivers are relatively rare.

We present, for the first time, CSES-1 beacon results based on two examples for daytime and nighttime. EIA (the northern crest) can be seen and located at ~20°N in the reconstructed image at 07:28 UTC on 20 July 2018 (daytime). Disturbances are shown in the reconstruction image at 18:40 UTC on 13 July 2018 (nighttime). Beacon measurements are found to be more consistent with ionosonde measurements than model results by comparing N_mF_2 at three sites at Lanzhou, Chongqing, and Kunming. Beacon measurements can be validated by their consistency with ionosonde measurements. Finally, we have studied VTEC variations from ground to ~500 km (the height of CSES-1 orbit) and ratios of VTEC between beacon measurements and CODE data. VTEC variation from ground to ~500 km has a range of 7.2–16.5 TECU for the daytime case and of 1.1–1.7 TECU for the nighttime case. The Beacon/CODE ratio of VTEC varies with latitude and time. The mean Beacon/CODE ratio is 0.69 for the daytime case and 0.26 for the nighttime case. The lower ratios of the nighttime case indicate higher altitudes of the ionosphere during nighttime, when the ionosphere is assumed to be a thin layer.

Acknowledgments

This research is supported by the "China Seismo-Electromagnetic Satellite (CSES)" project and the 13th Five-Year Technology Program (Grant No. 315030409). The authors thank ZhengZheng Ma for his help in evaluating this paper.

References

Austen, J. R., Franke, S. J., and Liu, C. H. (1988). Ionospheric imaging using computerized tomography. *Radio Sci.*, *23*(3), 299–307. https://doi.org/10.1029/RS023i003p00299

Bernhardt. P. A., Selcher, C. A., Basu, S., Bust, G., and Reising, S. (2000). Atmospheric studies with the tri-band beacon instrument on the COSMIC constellation. *Terr., Atmos. Oceanic Sci.*, *11*(1), 291–312. https://doi.org/10.3319/TAO.2000.11.1.291(COSMIC)

Bernhardt, P. A., and Siefring, C. L. (2006). New satellite-based systems for ionospheric tomography and scintillation region imaging. *Radio Sci.*, *41*(5), RS5S23. https://doi.org/10.1029/2005RS003360

Buonsanto, M. J. (1999). Ionospheric storms- a review. *Space Sci. Rev.*, *88*(3-4), 563–601. https://doi.org/10.1023/A:1005107532631

Chuo, Y. J., Liu, J. Y., Pulinets, S. A., and Chen, Y. I. (2002). The ionospheric perturbations prior to the Chi-Chi and Chia-Yi earthquakes. *J. Geodyn.*, *33*(4-5), 509–517. https://doi.org/10.1016/S0264-3707(02)00011-X

Dabas, R. S., Das, R. M., Sharma, K., and Pillai, K. G. M. (2007). Ionospheric precursors observed over low latitudes during some of the recent major earthquakes. *J. Atmos. Sol. Terr. Phys.*, *69*(15), 1813–1824. https://doi.org/10.1016/j.jastp.2007.09.005

Davies, K., and Baker, D. M. (1965). Ionospheric effects observed around the time of the Alaskan earthquake of March 28, 1964. *J. Geophys. Res.*, *70*(9), 2251–2253. https://doi.org/10.1029/JZ070i009p02251

Hsiao, T. Y., Tsai, L. C., and Liu, C. H. (2009). The initial results from the LITN of the FORMOSAT-3 TBB Program. *Terr. Atmos. Ocean. Sci.*, *20*(1), 261–271. https://doi.org/10.3319/TAO.2007.12.03.01(F3C)

Kunitsyn, V. E., Andreeva, E. S., Razinkov, O. G., and Tereshchenko, E. D. (1994). Phase and phase-difference ionospheric radio tomography. *Int. J. Imag. Syst. Technol.*, *5*(2), 128–140. https://doi.org/10.1002/ima.1850050209

Kunitsyn, V. E., and Tereshchenko, E. D. (2003). *Ionospheric Tomography*. Berlin, Heidelberg: Springer. https://doi.org/10.1007/978-3-662-05221-1

Leitinger, R., Schmidt, G., and Tauriainen, A. (1975). An evaluation method combining the differential Doppler measurements from two stations that enables the calculation of the electron content of the ionosphere. *J. Geophys.*, *41*(2), 201–213.

Leitinger, R. (1994). Data from orbiting navigation satellites for tomographic reconstruction. *Int. J. Imag. Syst. Technol.*, *5*(2), 86–96. https://doi.org/10.1002/ima.1850050205

Liperovskaya, E. V., Liperovsky, V. A., Silina, A. S., and Parrot, M. (2006). On spread-F in the ionosphere before earthquakes. *J. Atmos. Sol. Terr. Phys.*, *68*(2), 125–133. https://doi.org/10.1016/j.jastp.2005.10.005

Liu, J. Y., Chen, Y. I., Pulinets, S. A., Tsai, Y. B., and Chuo, Y. J. (2000). Seismo-ionospheric signatures prior to M≥6.0 Taiwan earthquakes. *Geophys. Res. Lett.*, *27*(19), 3113–3116. https://doi.org/10.1029/2000GL011395

Na, H. R. (1994). Computerized ionospheric tomography. *Int. J. Imaging Syst. Technol.*, *5*(2), 77–187.

Ondoh, T., and M. Hayakawa (1999). Anomalous occurrence of sporadic-E layers before the Hyogoken-Nanbu earthquake, M7.2 of January 17, 1995. In *Atmospheric and Ionospheric Electromagnetic Phenomena Associate with Earthquakes* (pp. 62–639). Tokyo: TERRAPUB.

Ou, M., Zhang, H. B., and Zhen, W. M. (2012). GPS-based Ionospheric Tomography with Constrained IRI as a Regularization. In *Proceedings of the 10th International Symposium on Antennas, Propagation & EM Theory* (pp. 656–659). Xian, China: IEEE. https://doi.org/10.1109/ISAPE.2012.6408856

Popov, K. V., Liperovsky, V. A., Meister, C. V., Biagi, P. F., Liperovskaya, E. V., and Silina, A. S. (2004). On ionospheric precursors of earthquakes in scales of 2-3 hours. *Phys. Chem. Earth*, *29*(4-9), 529–535. https://doi.org/10.1016/j.pce.2003.10.004

Pryse, S. E., and Kersley, L. (1992). A preliminary experimental test of ionospheric tomography. *J. Atmos. Terr. Phys.*, *54*(7-8), 1007–1012. https://doi.org/10.1016/0021-9169(92)90067-U

Pryse, S. E. (2003). Radio tomography: A new experimental technique. *Surv. Geophys.*, *24*(1), 1–38. https://doi.org/10.1023/A:1022272607747

Shen, X. H., Zhang, X. M., Wang, L. W., Chen, H. R., Wu, Y., Yuan, S. G., Shen, J. F., Zhao, S. F., Qian, J. D., and Ding, J. H. (2011). The earthquake-related disturbances in ionosphere and project of the first China seismo-electromagnetic satellite. *Earthq. Sci.*, *24*(6), 639–650. https://doi.org/10.1007/s11589-011-0824-0

Zhao, B. Q., Wang, M., Yu, T., Wan, W. X., Lei, J. H., Liu, L. B., and Ning, B. Q. (2008). Is an unusual large enhancement of ionospheric electron density linked with the 2008 great Wenchuan earthquake?. *J. Geophys. Res.*, *113*(A11), A11304. https://doi.org/10.1029/2008JA013613